

This is a pre print version of the following article:

Microstructured induced band pattern in Love wave propagation for novel nondestructive testing (NDT) procedures / Nobili, A.; Volpini, V.. - In: INTERNATIONAL JOURNAL OF ENGINEERING SCIENCE. - ISSN 0020-7225. - 168:(2021), pp. 103545-N/A. [10.1016/j.ijengsci.2021.103545]

Terms of use:

The terms and conditions for the reuse of this version of the manuscript are specified in the publishing policy. For all terms of use and more information see the publisher's website.

05/01/2026 02:26

Microstructured induced band pattern in Love wave propagation for novel non destructive testing (NDT) procedures

Abstract

We propose a new approach for assessing microstructural properties of materials via nondestructive testing (NDT). This approach lies on the observation that, accounting for the microstructure within the materials, reveals a nonclassical band propagation pattern for Love waves. Precisely this propagation structure may be directly related to the internal microstructure. To illustrate this, propagation of Love waves is first investigated within the linear theory of couple stress materials with micro-inertia. Proving wave existence by the argument principle provides a closed-form condition for propagation to occur. This connection defines propagation bands, whose limits correspond to the situation when Love waves move with the same speed as bulk waves in the underlying half-space (internal resonance). This condition is closely related to the layer-to-substrate microstructure and it may be used to assess either of the two. Furthermore, we show that the frequency equation is a three-term combination of antiplane Rayleigh and Rayleigh-Lamb functions (in a free and in a free/clamped plate). Consequently, investigation of any extra observable, such as Rayleigh waves, reduces the risk of multiple solutions at the signal processing stage. We finally consider the limit as either the half-space or the layer becomes classical elastic. We show that this unseemly bonding of dissimilar models, sometimes adopted in the literature, usually leads to inconsistencies.

Keywords: Love waves, Non destructive testing, Pass-bands, Internal resonance

1. Introduction

1 Love waves are antiplane waves localized near the free surface of a layer in
2 perfect contact with a half-space. These celebrated waves were first considered
3 by Love (1911) in a timely attempt to explain the defying appearance of an-
4 tiplane Rayleigh waves in seismograms, something that could not be achieved
5 in a homogeneous solid by the classical theory (Maugin, 1988; Gourgiotis and
6 Georgiadis, 2015). The absence of a wave component normal to the surface
7 makes Love waves especially attractive for NEMS and ultrasonic transducers
8 (Jin et al., 2005). Although Love waves have been studied in great detail in
9 the context of classical elasticity (Achenbach, 1984; Graff, 1991), no investiga-
10 tion is available that performs this analysis in the context of complex materials,
11 namely material models which account for microstructure. Besides, in recent
12 years there has been an increased interest in Love waves as potential candidates
13 for developing new non destructive testing (NDT) procedures, see Destuynder
14 and Fabre (2016) and references therein. Indeed, this approach falls in the wake
15 of existing successful applications in the field of defect detection for piezoelectric
16 ceramics (Jin et al., 2005). Also, consideration of multiple observables, beyond
17 the traditional Rayleigh waves, is capable of overcoming the well-known issue of
18 solution non-uniqueness at the signal post-processing stage, cf. Dal Moro (2020).

19 Couple stress theory is perhaps the simplest strain-gradient theory and it
20 aims to account for the discrete nature of materials at the micro-scale (Mindlin,
21 1964). Indeed, incorporating microstructural features inside classical elasticity
22 is a complex and yet important feat, for it allows to remediate many drawbacks
23 of the original theory. Among these, we mention the non-dispersive feature of
24 bulk and Rayleigh waves, the absence of antiplane Rayleigh waves, the impossi-
25 bility to predict a size for shear bands and the unbounded nature of stress near
26 defects, as in crack problems. A number of papers have investigated the way
27 microstructure alters such outcomes, through consideration of different com-
28 plex materials in the form of strain-gradient, micropolar, surface and non-local
29 elasticity. In their pioneering work, Graff and Pao (1967) studied plane strain

30 reflection of waves impinging onto a free surface of a couple stress solid in the
 31 absence of micro-inertia. They proved that waves propagate dispersively and
 32 possibly faster than Rayleigh waves. Shortly later, Sengupta and Ghosh (1974)
 33 investigated wave propagation in a couple stress layer. The first recognition
 34 that support of antiplane localized waves may be granted by "perturbation" of
 35 the classical boundary conditions is due to Maugin (1988). In particular, Var-
 36 doulakis and Georgiadis (1997) showed that introducing microstructural char-
 37 acteristics in the form of strain-gradient and surface-energy terms allows the
 38 theory to support antiplane Rayleigh waves only when accounting for a cer-
 39 tain type of gradient anisotropy. Ottosen et al. (2000) considered dispersion
 40 of Rayleigh waves in microstructured media which are described by the couple
 41 stress theory without micro-inertia. This work has been later extended by Geor-
 42 giadis and Velgaki (2003), where a number of insightful remarks are given with
 43 regard to the importance of considering rotational inertia for successfully re-
 44 producing results from lattice theories. Gourgiotis and Georgiadis (2015) show
 45 that antiplane Rayleigh and torsional waves are supported in a homogeneous
 46 half-space when a complete strain gradient theory is considered. Recently, No-
 47 bili et al. (2020) proved existence of a novel antiplane evanescent wave arising
 48 by mode conversion in couple stress elasticity with micro-inertia. It is precisely
 49 this wave that has been seen radiating energy away in the dynamic loading of
 50 a crack (Nobili et al., 2019).

51 The analysis is further complicated when two or more bodies are set in con-
 52 tact. Li et al. (2018) study reflection and transmission of plane strain thermo-
 53 elastic coupled waves in couple stress materials without micro-inertia. Wang
 54 et al. (2017) investigate plane strain reflection and transmission of elastic waves
 55 impinging onto a layer glued in between two couple stress half-spaces disregard-
 56 ing rotational inertia. Results are very involved and the limiting case of classical
 57 elastic half-spaces is also addressed. Recently, Nobili et al. (2021) considered
 58 propagation of Stoneley waves at the boundary between two couple stress half-
 59 spaces and found that incorporation of the microstructure greatly relaxes the
 60 classical restrictions for wave existence. In this paper, we show that this fea-

ture may be put to advantage to relate the band propagation structure to the underlying material microstructure.

We also address the not trivial situation where a couple stress body is bonded to a classical solid. Several contributions are available in the literature dealing with such layout. As an example, Fan and Xu (2018) considered Love waves arising on the surface of a couple stress layer bonded to a classical half-space, while Ray and Singh (2020) studied a couple stress stratum imperfectly bonded to a viscoelastic substrate. Since couple stress entails a kinematical description that is richer than classical elasticity's, the question of what boundary conditions are to be imposed is not trivial. The matter is settled in this paper by taking the proper limit of the general solution for Love waves localized in a couple stress layer perfectly bonded to a couple stress half-space in the presence of micro-inertia.

2. Variational derivation of couple stress elasticity

We begin by considering microstructural features within our description of elastic materials. For this, as it occurs in polar materials, we supplement the classical displacement field \mathbf{u} by the micro-rotation field $\boldsymbol{\varphi}$ as the kinematical fundamental variables. However, in contrast to Cosserat micro-polar theories, wherein displacements and micro-rotations are independent fields, couple stress (CS) theory relates one to the other, through the connection

$$\boldsymbol{\varphi} = \frac{1}{2} \text{curl } \mathbf{u}. \quad (1)$$

Component-wise, this reads $\varphi_i = \frac{1}{2} E_{ijk} u_{k,j}$, where $i, j, k \in \{1, 2, 3\}$, E_{ijk} is the alternator tensor and Einstein's summation convention on twice repeated subscripts is assumed. Hereinafter, a subscript comma denotes partial differentiation, e.g. $(\text{grad } u_k)_j = u_{k,j} = \partial u_k / \partial x_j$, while subscript round brackets produce symmetrization, i.e. $u_{(i,j)} = (u_{i,j} + u_{j,i})/2$. Alongside the linear strain tensor $\boldsymbol{\varepsilon}$ commonly defined in classical elasticity (CE)

$$\varepsilon_{ij} = u_{(i,j)}, \quad (2)$$

we introduce the *torsion-flexure (wryness or curvature) tensor* χ

$$\chi_{ij} = \varphi_{i,j}, \quad (3)$$

that, in light of the connection (1), is purely deviatoric, i.e. $\chi = \chi^D$, being $\chi^D = \chi - \frac{1}{3}(\text{tr } \chi)\mathbf{1}$, where $\mathbf{1}$ is the rank-2 identity tensor and $\text{tr } \chi = \chi \cdot \mathbf{1}$ the trace operator. Here, a dot denotes the scalar product, i.e. $\chi \cdot \mathbf{1} = \chi_{ii}$; in particular, in the case of vectors, it induces the natural norm $\mathbf{u}^2 = \|\mathbf{u}\|^2 = \mathbf{u} \cdot \mathbf{u}$.

We define the action integral for the deformable body \mathcal{B} in the time frame $[0, t]$

$$\mathcal{A} = - \int_0^t \mathcal{L} d\tau,$$

having introduced the Lagrangian function $\mathcal{L} = \mathcal{K} - \mathcal{V}$ as the difference between the kinetic and the potential energy. For the former, we take

$$\mathcal{K} = \int_{\mathcal{B}} \left(\frac{1}{2} \rho \dot{\mathbf{u}}^2 + \frac{1}{2} J \dot{\boldsymbol{\varphi}}^2 \right) dV,$$

where ρ and J are the mass- and the micro-inertia densities, respectively. Hereinafter, a superposed dot denotes time differentiation, i.e. $\dot{\mathbf{u}} = \partial \mathbf{u} / \partial t$. In the absence of body forces, the potential energy reads

$$\begin{aligned} \mathcal{V} = \int_{\mathcal{B}} \left[\frac{1}{2} \boldsymbol{\sigma} \cdot \boldsymbol{\varepsilon} + \frac{1}{2} \boldsymbol{\mu}^T \cdot \boldsymbol{\chi} + \boldsymbol{\pi} \cdot \left(\boldsymbol{\varphi} - \frac{1}{2} \text{curl } \mathbf{u} \right) \right] dV \\ - \int_{\partial \mathcal{B}} (\mathbf{p}_n \cdot \mathbf{u} + \mathbf{q}_n \cdot \boldsymbol{\varphi}) dA, \end{aligned} \quad (4)$$

and the superscript T , denoting transposition, is introduced for compatibility with Koiter (1964). The surface integral in (4) accounts for externally applied force and couple stress tractions, respectively \mathbf{p}_n and \mathbf{q}_n .

As in CE, conjugated to the strain tensor $\boldsymbol{\varepsilon}$ is the Cauchy (or force) stress tensor, \mathbf{t} , which is generally non-symmetric. Consequently, it may be decomposed into its symmetric and skew-symmetric part, respectively

$$\sigma_{ij} = t_{(ij)}, \quad \tau_{ij} = t_{ij} - \sigma_{ij}.$$

Since $\boldsymbol{\varepsilon}$ is symmetric, only $\boldsymbol{\sigma}$ really performs work.

98 Conjugated to the curvature tensor χ is the couple stress tensor $\boldsymbol{\mu}$, which, in
 99 general, performs work through all its components. However, it should be noted
 100 that χ is deviatoric, whence only the deviatoric part of $\boldsymbol{\mu}^D$ really matters. As a
 101 result, to any effect, $\boldsymbol{\mu}$ may be replaced by its deviatoric part $\boldsymbol{\mu}^D$. Indeed, this
 102 theory is sometimes named indeterminate after the observation that the first
 103 invariant of the couple stress tensor rests indeterminate. Consequently, it may
 104 be set equal to zero without any loss of generality, e.g. $\text{tr } \boldsymbol{\mu} = 0$. For the sake
 105 of brevity, in the following we shall write $\boldsymbol{\mu}$, with the understanding that $\boldsymbol{\mu}^D$ is
 106 meant. For any surface of unit normal \boldsymbol{n} , the tensor $\boldsymbol{\mu}$ determines the internal
 107 reduced couple vector $\bar{\boldsymbol{q}} = \boldsymbol{\mu}^T \boldsymbol{n}$ acting across that surface.

Finally $\boldsymbol{\pi}$ is a Lagrange multiplier enforcing the kinematical constraint (1)
 and allowing \boldsymbol{u} and $\boldsymbol{\varphi}$ to be varied independently. For it, we let $\boldsymbol{\pi} = -2 \text{ axial } \boldsymbol{\tau}$,
 with $(\text{axial } \boldsymbol{\tau})_i = \frac{1}{2} E_{ijk} \tau_{jk}$ denoting the axial vector attached to the skew-
 symmetric stress \boldsymbol{t} (in Nobili et al. (2020) we dispensed with the factor 2 in the
 definition of the axial vector). With this definition, we have

$$\text{axial } \boldsymbol{\tau} = [\tau_{23}, \tau_{31}, \tau_{12}],$$

108 and the inverse formula $E_{ijk}(\text{axial } \boldsymbol{\tau})_k = \tau_{ij}$.

Component-wise, the Lagrangian volumetric density reads

$$\mathcal{L} = \frac{1}{2} \rho \dot{u}_i \dot{u}_i + \frac{1}{2} J \dot{\varphi}_i \dot{\varphi}_i - \frac{1}{2} \sigma_{ij} u_{i,j} - \frac{1}{2} \mu_{ji} \varphi_{i,j} - \pi_i \left(\varphi_i - \frac{1}{2} e_{ijk} u_{k,j} \right).$$

By Hamilton's principle, the problem's governing equations are the Euler-Lagrange equations for the action integral. In the absence of body forces, they read

$$\text{div } \boldsymbol{t} = \rho \ddot{\boldsymbol{u}}, \quad (5a)$$

$$2 \text{ axial } \boldsymbol{\tau} + \text{div } \boldsymbol{\mu} = J \ddot{\boldsymbol{\varphi}}, \quad (5b)$$

109 it being $\text{div } \boldsymbol{t} = t_{ji,j}$. Application of the permutation tensor to Eq.(5b) yields

$$\boldsymbol{\tau} = -\frac{1}{2} \mathbf{E} (\text{div } \boldsymbol{\mu} - J \ddot{\boldsymbol{\varphi}}), \quad (6)$$

110 whence the skew-symmetric part of the force stress tensor \boldsymbol{t} is determined by
 111 rotational equilibrium, beside any constitutive consideration. It follows that

Eq.(6) is generally not objective (Ottosen et al., 2000; Gourgiotis et al., 2013), although, for time-harmonic motions, this is no longer an issue (Shodja et al., 2015).

2.1. Antiplane deformations

Under antiplane deformations, the displacement field $\mathbf{u} = [u_1, u_2, u_3]$ is completely defined by the out-of-plane component $u_3 = u_3(x_1, x_2, t)$. Then, the non-zero components of the micro-rotation vector, of the strain and of the curvature tensor become (see Nobili et al. (2019, 2020, 2021))

$$\varphi_1 = \frac{1}{2}u_{3,2}, \quad \varphi_2 = -\frac{1}{2}u_{3,1}, \quad (7a)$$

$$\varepsilon_{13} = \frac{1}{2}u_{3,1}, \quad \varepsilon_{23} = \frac{1}{2}u_{3,2}, \quad (7b)$$

$$\chi_{11} = -\chi_{22} = \frac{1}{2}u_{3,12}, \quad \chi_{21} = -\frac{1}{2}u_{3,11}, \quad \chi_{12} = \frac{1}{2}u_{3,22}. \quad (7c)$$

Consequently, Eqs.(5) simplifies to

$$\sigma_{13,1} + \sigma_{23,2} + \tau_{13,1} + \tau_{23,2} = \rho \ddot{u}_3, \quad (8a)$$

$$\mu_{11,1} + \mu_{21,2} + 2\tau_{23} = J \ddot{\varphi}_1, \quad (8b)$$

$$\mu_{12,1} + \mu_{22,2} - 2\tau_{13} = J \ddot{\varphi}_2. \quad (8c)$$

For hyperelastic materials, a stored energy potential $U = U(\boldsymbol{\varepsilon}, \boldsymbol{\chi})$ exists which connects the strain $\boldsymbol{\varepsilon}$ and the curvature $\boldsymbol{\chi}$ to the Cauchy stress and to the couple stress. Indeed, we have

$$\boldsymbol{\sigma} = \frac{\partial U}{\partial \boldsymbol{\varepsilon}}, \quad \boldsymbol{\mu}^T = \frac{\partial U}{\partial \boldsymbol{\chi}},$$

which, to leading order for small deformations of an isotropic material, yield

$$\boldsymbol{\sigma} = 2G\boldsymbol{\varepsilon} + \Lambda(\text{tr } \boldsymbol{\varepsilon})\mathbf{1}, \quad \boldsymbol{\mu} = 2Gl^2 (\boldsymbol{\chi}^T + \eta\boldsymbol{\chi}). \quad (9)$$

Here, Λ and $G > 0$ are the classical Lamé moduli, with $3\Lambda + 2G > 0$. Also, $l > 0$ is a characteristic length connected to the microstructure and $-1 < \eta < 1$ is a dimensionless number similar to Poisson's ratio. The material parameters l and η may be determined experimentally as in Lakes (1986). The situation $\eta = 0$ corresponds to the strain gradient effect considered in Zhang et al. (1998),

122 while the limiting value $\eta = 1$ corresponds to the modified couple stress theory of
 123 elasticity introduced in Yang et al. (2002) via the balance of torques of torques.

The constitutive equations (9), in light of the definitions (2,3) and with the help of the kinematic relations (7), give the force stress and the couple stress in terms of the u_3 displacement alone (Nobili et al., 2019)

$$\sigma_{13} = Gu_{3,1}, \quad \sigma_{23} = Gu_{3,2}, \quad (10a)$$

$$\mu_{11} = -\mu_{22} = Gl^2(1 + \eta)u_{3,12}, \quad \mu_{21} = Gl^2(u_{3,22} - \eta u_{3,11}), \quad (10b)$$

$$\mu_{12} = -Gl^2(u_{3,11} - \eta u_{3,22}). \quad (10c)$$

124 Introducing Eqs.(7a,10) into (6) yields

$$\tau_{13} = -\frac{1}{2}Gl^2\hat{\Delta}u_{3,1} + \frac{J}{4}\ddot{u}_{3,1}, \quad \tau_{23} = -\frac{1}{2}Gl^2\hat{\Delta}u_{3,2} + \frac{J}{4}\ddot{u}_{3,2}, \quad (11)$$

125 which correspond to Eqs.(9) of Mishuris et al. (2012). Here, $\hat{\Delta}$ denotes the 2-D
 126 Laplace operator in the dimensional co-ordinates (x_1, x_2) . Finally, Eqs.(10a)
 127 and (11) allow to rewrite translational equilibrium (8a) as the meta biharmonic
 128 equation

$$G\left(\frac{1}{2}l^2\hat{\Delta}\hat{\Delta}u_3 - \hat{\Delta}u_3\right) - \frac{J}{4}\hat{\Delta}\ddot{u}_3 + \rho\ddot{u}_3 = 0. \quad (12)$$

129 2.2. Boundary conditions

Accounting for surface terms in Hamilton's principle gives the boundary conditions

$$\mathbf{p} = \mathbf{p}_n, \quad \text{and} \quad \mathbf{q} = \mathbf{q}_n,$$

where we have let the reduced traction and reduce couple stress vectors, respectively

$$\mathbf{p} = \mathbf{t}^T \mathbf{n} + \frac{1}{2} \text{grad } \mu_{nn} \times \mathbf{n}, \quad (13a)$$

$$\mathbf{q} = \boldsymbol{\mu}^T \mathbf{n} - \mu_{nn} \mathbf{n}. \quad (13b)$$

130 Here, $\mu_{nn} = \mathbf{n} \cdot \boldsymbol{\mu} \mathbf{n}$ is the normal component of the couple stress traction vector.
 131 Eq.(13b) shows that only the tangential part of the couple stress vector may be
 132 prescribed. Indeed, it can be proved that the normal component of the couple
 133 stress tension is precisely annihilated by the second term in (13a), see also Koiter
 134 (1964) and Ottosen et al. (2000).

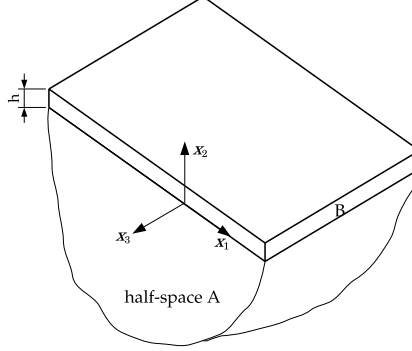


Figure 1: An infinite layer (B) perfectly bonded to an elastic half-space (A). The half-space is often named the substrate

2.3. Nondimensionalization and time harmonic motions

Let us consider a Cartesian co-ordinate system (O, x_1, x_2, x_3) and a layer, $\mathcal{B}_B = \{(x_1, x_2, x_3) : 0 < x_2 < h\}$, in perfect contact with the half-space $\mathcal{B}_A = \{(x_1, x_2, x_3) : x_2 < 0\}$, see Fig.1. The layer and the half-space are made of generally different isotropic elastic couple stress (CS) materials, for which antiplane deformations are considered.

At the layer top face, $x_2 = h$, it is $\mathbf{n} = [0, 1, 0]$ and, according to Eqs.(13), the out-of-plane component of the reduced force traction and the in-plane components of the couple stress traction read, respectively,

$$p_3 = (t_{23} + \frac{1}{2}\mu_{22,1}), \quad \text{and} \quad q_1 = \mu_{21}, \quad q_2 = 0. \quad (14)$$

We introduce the reference length Θl , by which we scale the spatial coordinates $(\xi_1, \xi_2, \xi_3) = (x_1, x_2, x_3)(\Theta l)^{-1}$ and the layer thickness $H = h/l$. In the same manner, we let the reference time $T = l/\tilde{c}_s$ and the dimensionless time $\tau = t/T$. Here, $\tilde{c}_s = \sqrt{G/\rho}$ is the bulk shear wave speed of CE. The parameter Θ is a convenient factor that is introduced so as to simplify notation. The equilibrium equation (12) becomes

$$\Delta \Delta u_3 - 2\Theta^2 \Delta u_3 - 2\Theta^4 \left(\frac{\ell^2}{\Theta^2} \Delta u_{3,\tau\tau} - u_{3,\tau\tau} \right) = 0, \quad (15)$$

where Δ is the 2-D Laplace operator in ξ_1 and ξ_2 and we have let the dynamic

151 characteristic length (Mishuris et al., 2012)

$$\ell = \frac{l_d}{l}, \quad \text{with} \quad l_d = \frac{1}{2} \sqrt{\frac{J}{\rho}}.$$

152 The latter is proportional to $2\sqrt{6}l_d$, that is introduced in Shodja et al. (2015).

153 Consideration of time-harmonic solutions brings

$$u_3 = W(\xi_1, \xi_2) \exp(-i\Omega\tau),$$

154 where i is the imaginary unit and $\Omega = \omega T > 0$ the dimensionless (time) fre-
 155 quency. Then, Eq.(15) yields the meta biharmonic PDE (Georgiadis and Vel-
 156 gaki, 2003, Eq.(19)) for the wave amplitude W :

$$[\Delta\Delta - 2(1 - \ell^2\Omega^2)\Theta^2\Delta - 2\Omega^2\Theta^4] W = 0. \quad (16)$$

157 This homogeneous equation is easily factored

$$(\Delta + \delta^2)(\Delta - 1)W = 0, \quad (17)$$

158 provided that Θ is let as in (Nobili et al., 2020, Eq.(3.4))

$$\Theta^2 = \frac{\sqrt{(1 - \ell^2\Omega^2)^2 + 2\Omega^2} - 1 + \ell^2\Omega^2}{2\Omega^2} \quad (18)$$

159 We then have (Nobili et al., 2021, Eq.(21))

$$\delta = 2\delta_{cr}\Theta^2, \quad \text{with} \quad \delta_{cr} = \ell_{cr}\Omega, \quad \ell_{cr} = 1/\sqrt{2}. \quad (19)$$

160 Eq.(17) is especially convenient for it shows that two (antiplane) bulk modes are
 161 supported: one, travelling, having wavenumber $\kappa = \pm\delta$, and another, evanes-
 162 cent, possessing wavenumber $\kappa = \pm i$ (Nobili et al., 2020).

In dimensionless form, the traction vectors (14) become

$$p_3 = -\frac{G}{2\Theta^3} [(\delta^2 - 1)W_{,2} + (\eta + 2)W_{,112} + W_{,222}], \quad (20a)$$

$$q_1 = \frac{Gl}{\Theta^2} (W_{,22} - \eta W_{,11}). \quad (20b)$$

163 *2.4. Extension to two materials*

164 We now consider the fact that A and B are constituted by different isotropic
 165 homogeneous materials, each having the relevant classical shear wave speed
 166 $\tilde{c}_{sA,B} = \sqrt{G_{A,B}/\rho_{A,B}}$. We can now choose to bring the problem in dimen-
 167 sionless form against either of the two materials: to fix ideas, we refer to the
 168 half-space A and let

$$l = l_A, \quad \text{and} \quad T = T_A = l_A/\tilde{c}_{sA},$$

whence $\Omega = \omega T_A$. Therefore, one should remember that, unless otherwise spec-
 ified, reference to the microstructure of A is made through the dimensionless
 variables. In order to move from A to B, we introduce the ratios

$$\beta = l_B/l_A, \quad v = T_A/T_B.$$

169 With these, we can introduce the dimensionless wavenumber $\kappa_B = \beta\kappa$ and
 170 frequency $\Omega_B = \omega T_B = \Omega/v$, both being normalized with respect to B. The
 171 limiting case when B is classical elastic, i.e. in the absence of microstructure for
 172 B, can be retrieved by taking

$$v \rightarrow +\infty, \quad \beta \rightarrow 0, \quad \text{such that} \quad \beta v = \frac{\tilde{c}_{sB}}{\tilde{c}_{sA}} < \infty. \quad (21)$$

173 The corresponding limit where A is deprived of microstructure may be obtained
 174 taking $\beta \rightarrow \infty$, with $\beta v < \infty$ and making use of variables normalised with
 175 respect to B.

We let the dynamic characteristic lengths of A and B

$$\ell_{A,B} = l_{dA,B}/l_{A,B},$$

176 being $l_{dA,B} = \frac{1}{2}\sqrt{J_{A,B}/\rho_{A,B}}$. Besides, we define the equivalent of δ for B,
 177 cf.(Nobili et al., 2021, Eq.(24))

$$\frac{\psi}{v} = \frac{\sqrt{(1 - \ell_B^2 \Omega_B^2)^2 + 2\Omega_B^2 - 1 + \ell_B^2 \Omega_B^2}}{\sqrt{2}\Omega_B}. \quad (22)$$

Indeed, $\psi = \delta$ when $\ell_B = \ell_A$ and $v = 1$. Also, $\delta \sim \psi \sim \Omega/\sqrt{2}$ and $\Theta \sim 2^{-1/2}$ as $\Omega \rightarrow 0$. For ψ we have the asymptotics

$$\psi \rightarrow \sqrt{2}\Omega\ell_B + O(v^2), \quad \text{as } v \rightarrow 0,$$

178 and

$$\psi \rightarrow \delta_{cr} + O(v^{-2}), \quad \text{as } v \rightarrow +\infty. \quad (23)$$

179 The governing equation (16) specializes to

$$(\Delta + \delta^2)(\Delta - 1)W_A = 0, \quad (\xi_1, \xi_2) \in \mathcal{B}_A, \quad (24)$$

180 for the half-space A, and to

$$(\Delta + \delta_1^2)(\Delta - \delta_2^2)W_B = 0, \quad (\xi_1, \xi_2) \in \mathcal{B}_B, \quad (25)$$

for the layer B. Clearly, W_A and W_B are the solution amplitudes in medium A and B, respectively. Also, we have let the dimensionless wavenumbers

$$\delta_{1,2} = \frac{\kappa_{1,2}}{\beta}, \quad \text{with } \kappa_1 = \frac{\sqrt{\delta\psi}}{v}, \quad \kappa_2 = \sqrt{\delta/\psi},$$

181 normalized with respect to $\Theta\ell_A$ and $\Theta\ell_B$, respectively. They correspond to bulk
182 travelling and evanescent modes for B. With this notation, we can easily express
183 the corresponding bulk wave phase speed with respect to \tilde{c}_{sA} or \tilde{c}_{sB}

$$c_{SH} = V_{A,B}\Theta\tilde{c}_{sA,B},$$

where we have let the dimensionless phase speed

$$V_A = \frac{\Omega}{\delta}, \quad \text{and} \quad V_B = \frac{\Omega_B}{\kappa} = \frac{\Omega}{v\kappa}.$$

184 In fact, we see that, in the limit (21), $V_B = \Theta^{-1}$ for $\kappa = \kappa_1$, which gives the
185 classical bulk wavespeed $c_{SH} = \tilde{c}_{sB}$. For $\kappa = \kappa_2$, $V_B \rightarrow 0$ and the evanescent
186 bulk mode becomes standing, as already pointed out in Nobili et al. (2019). We
187 have the Short-Wave High-Frequency (SWHF) approximation for bulk waves

$$\kappa^2 - 2\ell_A^4\Omega^2 = 0. \quad (26)$$

For material B, the boundary tractions (20) become (Nobili et al., 2021, Eqs.(27))

$$p_{3B} = -\frac{G_B}{2\Theta^3} \left\{ \beta^2 [(\eta_B + 2) W_{B,112} + W_{B,222}] + \frac{\delta}{\psi} \left(\frac{\psi^2}{v^2} - 1 \right) W_{B,2} \right\}, \quad (27a)$$

$$q_{1B} = \frac{G_B l_B}{\Theta^2} \beta^2 (W_{B,22} - \eta_B W_{B,11}), \quad (27b)$$

188 which, in the limiting case (21) and using of Eqs.(19,23), lends the classical
189 limit.

190 3. Dispersion relation for Love waves

191 For guided propagation along ξ_1 , we have (recall we chose $l = l_A$)

$$W_{A,B}(\xi_1, \xi_2) = l w_{A,B}(\xi_2) \exp(\imath \kappa \xi_1),$$

where $K = kl$ denotes the dimensionless (spatial) wavenumber in the propagation direction ξ_1 . Letting $V = \Omega/K$, we get the dimensional phase speed in the propagation direction

$$c = \omega/k = V \tilde{c}_{sA}.$$

192 The general decaying solution of Eq.(24), valid for the half-space A, reads

$$w_A(\xi_2) = s_1 \exp(A_1 \xi_2) + s_2 \exp(A_2 \xi_2), \quad (28)$$

193 where $s_{1,2}$ are undetermined amplitudes and

$$A_1 = \sqrt{\kappa^2 - \delta^2}, \quad A_2 = \sqrt{\kappa^2 + 1}, \quad (29)$$

194 are the decay indices in the thickness direction ξ_2 . For decay to occur, we need
195 to give proper and definite meaning to the square root multivalued function
196 (Noble, 1958). This is obtained introducing the cut complex plane and choosing
197 the particular branch of the square root such that $A_{1,2}(\kappa) \rightarrow |\kappa|$ as $\kappa \rightarrow \infty$ on
198 the real axis (Nobili et al., 2019). Cuts start at the branch points $\pm\delta$ and move
199 in opposing direction away from the real axis. As a result, $A_1(\kappa)$ is real positive
200 on the real domain $|\kappa| > \delta$, and $A_2(\kappa)$ is real positive on the whole real axis.

Similarly, we let

$$B_1 = \sqrt{\kappa^2 - \delta_1^2}, \quad B_2 = \sqrt{\kappa^2 + \delta_2^2},$$

and the general solution of Eq.(25) is given by Nobili et al. (2020)

$$w_B(\xi_2) = e_1 \cosh(B_1 \xi_2) + e_2 \cosh(B_2 \xi_2) \\ + o_1 B_1^{-1} \sinh(B_1 \xi_2) + o_2 B_2^{-1} \sinh(B_2 \xi_2), \quad (30)$$

201 where the dimensionless wavenumbers in the thickness direction ξ_2 are $P = \imath B_1$
 202 and $Q = \imath B_2$. Indeed, going back to the dimensional co-ordinate x_2 , we have
 203 $(p, q) = (P, Q)/(l\Theta)$ and

$$(p, q) = -k^2 \pm \frac{1}{l^2} \left(\sqrt{1 + 2l^2 \omega^2 c_{sA}^{-2}} - 1 \right),$$

204 which correspond to (3.5.1) and (3.5.2) of Fan and Xu (2018)¹.

205 3.1. Rayleigh function

206 Antiplane surface travelling waves (Rayleigh waves) occur in correspondence
 207 of the real zeros of the Rayleigh function (Nobili et al., 2021, §4.1)

$$R_0(\kappa, \lambda_1, \lambda_2, \eta) = (\eta \kappa^2 - \lambda_1 \lambda_2)^2 - \lambda_1 \lambda_2 (\lambda_1 + \lambda_2)^2, \quad (31)$$

that is analytic in the cut complex plane. This form of the Rayleigh function is especially simple, and it may be specialized for either A or B upon introducing the corresponding decay indices for $\lambda_{1,2}$ and microstructure ratio η . For example, it can be specialized for A

$$R_A(\kappa) = R_0(\kappa, A_1, A_2, \eta_A)$$

to give the form already adopted in Nobili et al. (2019, 2020)

$$(A_1 - A_2)R_A(\kappa) = \zeta_{11A}^2 A_1 - \zeta_{12A}^2 A_2,$$

208 having let $\zeta_{11A} = \eta_A \kappa^2 + A_2^2$ and $\zeta_{12A} = \eta_A \kappa^2 + A_1^2$.

¹Provided that we replace ℓ with $\sqrt{2}\ell$ and take the opposite of q^2

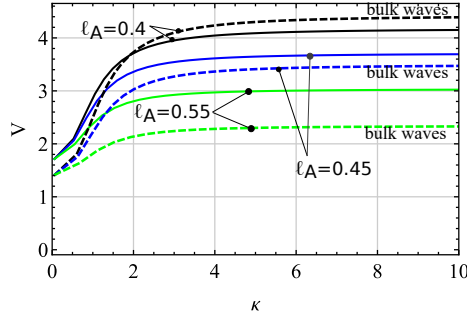


Figure 2: Dispersion curves for Rayleigh waves in medium B (solid) compared to bulk waves in medium A (dashed curves) with the parameters $\ell_A = 0.4$ (black), $\ell_A = 0.45$ (blue) and $\ell_A = 0.55$ (green). It appears that only in the case $\ell_A = 0.4$, bulk waves move faster than Rayleigh waves in the short-wave regime

Existence and uniqueness of antiplane Rayleigh waves is proved by the argument principle in Nobili et al. (2021), where it is also shown that the Rayleigh root is the single real zero of a bi-quartic polynomial equation which is regularly perturbed in η_A . Indeed, for $\eta_A = 0$, we have $\kappa = \pm\delta_1$ whence, in general, we can write the solution as a power series in η_A

$$\kappa_R^2 = \delta_1^2 \left(1 + \frac{\delta_1^6}{(\delta_1^2 + \delta_2^2)^3} \eta_A^4 + \dots \right). \quad (32)$$

This expansion, once specialized for A and up to first order correction terms in η_A , corresponds to (Nobili et al., 2020, Eq.(3.37)). From (32) follows the SWHF approximation

$$\kappa^2 - 2\Omega^2 \frac{\ell_A^2 \ell_B^2}{\beta^2 v^2} (1 + \eta_A^4 + \dots) = 0, \quad (33)$$

which provides the asymptotic limit for antiplane Rayleigh-Lamb (RL) modes.

Hereinafter, numerical exploration is presented for the parameter set $\ell_B = 0.5$, $\beta = v = 1.1$, $H = 0.1$, $\eta_A = 0.8$ and $\eta_B = 0.5$. Fig.2 plots the dispersion curves for Rayleigh waves in the layer B, superposed onto bulk waves in medium A. It appears that, when micro-inertia in A is small enough, bulk waves in A move faster than Rayleigh waves in B.

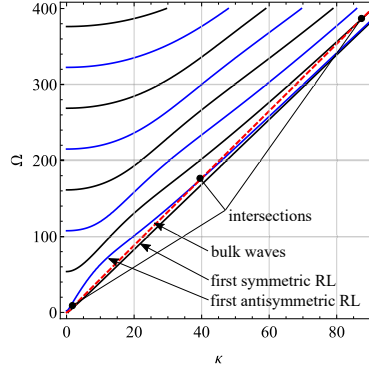


Figure 3: Frequency spectrum branches for symmetric (solid, black) and antisymmetric (solid, blue) Rayleigh-Lamb waves, with $\ell_A = 0.4$. The spectrum of bulk waves in medium A (dashed, red) intersects RL modes in an infinite succession of points. These are cut-on/cut-off points for Lamb waves.

3.2. Antiplane Rayleigh-Lamb waves in a free plate

Guided propagation in the free layer is described by the RL frequency equation

$$D_{RL}(\kappa) = d_s(\kappa)d_o(\kappa), \quad (34)$$

where $d_s(\kappa)$ and $d_o(\kappa)$ are given in Nobili et al. (2020) respectively for symmetric and anti-symmetric modes. Looking at them, it is clear that $D_{RL}(\kappa)$ depends on B_1 and B_2 through even powers and therefore it is *analytic in the whole complex plane*, i.e. it is holomorphic. Physically, this means that there are no bulk waves associated to RL propagation. Eq.34 may be rewritten in terms of the Rayleigh function

$$D_{RL}(\kappa) = \frac{(B_1 - B_2)^2}{8B_1B_2} R_B(\kappa)^2 \left[\cosh\left(\frac{H(B_1 + B_2)}{\Theta}\right) - 1 \right] - \frac{(\zeta_{11B}^2 B_1 + \zeta_{12B}^2 B_2)^2}{8B_1B_2} \left[\cosh\left(\frac{H(B_1 - B_2)}{\Theta}\right) - 1 \right], \quad (35)$$

whence we retrieve the well-known result that, when it comes to very short waves, the layer behaves just like a half-space.

Fig.3 plots the frequency spectrum for antiplane RL symmetric and antisymmetric waves in medium B, cfr. Nobili et al. (2020). In this Figure, RL branches are superposed onto the spectrum for SH bulk waves in medium A, and it ap-

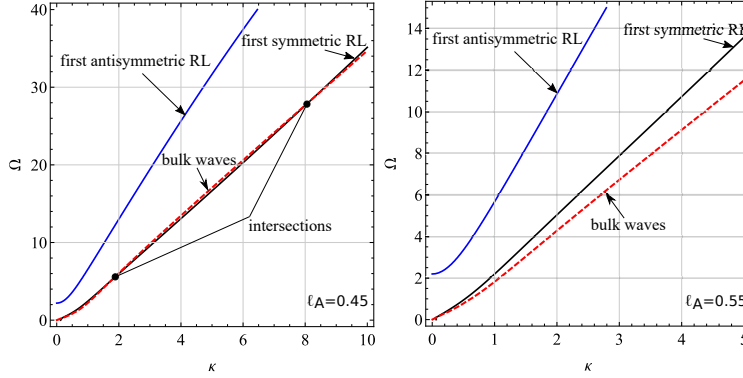


Figure 4: Frequency spectrum branches for symmetric (solid, black) and antisymmetric (solid, blue) Rayleigh-Lamb waves, with $\ell_A = 0.45$ (left) and $\ell_A = 0.55$ (right), superposed onto the spectrum of bulk waves in medium A (dashed, red). In the first case we have two intersections, in the second none.

pears that a infinite succession of intersection points occur, alternatively with symmetric and antisymmetric branches. These points are given by

$$D_{RL}(\delta) = 0,$$

and represent propagation states for which RL waves in medium B coexist with bulk waves in medium A (or, equally, they have the same phase speed).

In contrast, when micro-inertia in medium A increases, we move to two intersections and, eventually, to none, as it is illustrated in Figs.4. The two intersection condition is remarkable given that it occurs with the same first symmetric branch, i.e. there are two propagation frequencies that support longitudinal waves in the layer and also in the half-space. The regime shift from an infinite to a finite number of intersections occurs when the phase speed of Rayleigh waves in medium B becomes greater than that of bulk waves in medium A, as demonstrated in Fig.2. Therefore, comparing expansion (26) with (33), an approximate criterion for existence of an infinite number of intersections may be obtained

$$\ell_{0A} < \frac{\ell_{0B}}{\beta v}. \quad (36)$$

For example, with the parameter set of Fig.2, we get $\ell_{0A} < 0.41$. This criterion may be improved for large values of η_A by taking into consideration more terms

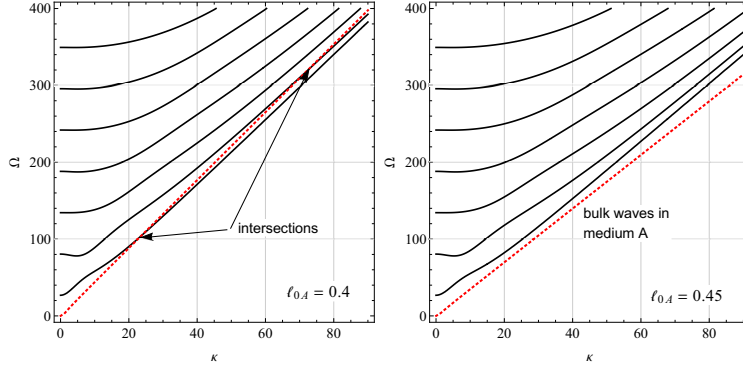


Figure 5: Frequency spectrum for Rayleigh-Lamb waves in a free/clamped plate, with $\ell_A = 0.4$ (left) and $\ell_A = 0.45$ (right). The frequency spectrum of bulk waves in medium A is also plotted (dotted, red) and it intersects RL modes only in the case $\ell_A = 0.4$

in the expansions.

3.3. Rayleigh-Lamb waves in a clamped-free plate

Proceeding as in Nobili et al. (2020), it can be proved that propagation in a free/clamped (FC) layer occurs according to the holomorphic function

$$D_{FC}(\kappa) = \frac{1}{2} \frac{(B_1 - B_2)^2}{B_1 B_2} R_B(\kappa) \left[\cosh \left(\frac{H(B_1 + B_2)}{\Theta} \right) - 1 \right] - (\zeta_{11B} - \zeta_{12B})^2 - \frac{1}{2} (B_2^{-1} + B_1^{-1}) (\zeta_{11B}^2 B_1 + \zeta_{12B}^2 B_2) \left[\cosh \left(\frac{H(B_1 - B_2)}{\Theta} \right) - 1 \right]. \quad (37)$$

In the SWHF approximation, the first term of $D_{FC}(\kappa)$ grows exponentially and dominates, whence propagation occurs through Rayleigh waves, just as in a half-space.

Fig.5 compares RL spectra in a free/clamped plate with bulk modes for medium A. Again, we see that an infinite succession of intersection points between the two is possible inasmuch as the phase speed of Rayleigh waves in medium B is lower than that of bulk waves in medium A, which requirement is approximated by Eq.(36). Indeed, increasing rotational inertia in medium A, intersections are no longer possible, while a finite number of intersections (as it occurs for RL waves) is not supported.

At the layer/half-space joining surface, we impose perfect adhesion

$$w_A(0) = w_B(0), \quad (38a)$$

$$w'_A(0) = w'_B(0), \quad (38b)$$

$$p_{3A}(0) = p_{3B}(0), \quad (38c)$$

$$q_{1A}(0) = q_{1B}(0), \quad (38d)$$

while the layer top surface $\xi_2 = H/\Theta$ is subjected to free conditions

$$p_{3B}(\Theta^{-1}H) = 0, \quad (39a)$$

$$q_{1B}(\Theta^{-1}H) = 0. \quad (39b)$$

Introducing the solutions (28,30) into the boundary conditions (39,38) yields a homogeneous system of linear equations in the unknown amplitudes $e_{1,2}$, $o_{1,2}$, $s_{1,2}$, which admits non-trivial solutions inasmuch as the *secular (or frequency)* equation

$$\Delta(\kappa) = 0,$$

255 is satisfied. Letting $\Gamma = G_B/G_A$, the ratio of the layer to the half-space shear
256 moduli, the general form of the secular equation can be written as

$$\Delta(\kappa) = \beta^6 \Gamma^2 (A_1 - A_2) D_0(\kappa),$$

257 having let the quadratic polynomial in Γ

$$D_0(\kappa) = d_0 + d_1 \Gamma + d_2 \Gamma^2, \quad (40)$$

with

$$d_0 = -\beta^{-2} R_A(\kappa) D_{FC}(\kappa),$$

$$d_1 = D_1(\kappa),$$

$$d_2 = -4\beta^2 D_{RL}(\kappa).$$

Here, $D_1(\kappa)$ expresses the coupling between the half-space and the layer

$$D_1(\kappa) = (B_1 - B_2)R_B(\kappa) \left\{ c_+ \left[\cosh \left(\frac{H(B_1 + B_2)}{\Theta} \right) - 1 \right] - \frac{s_+}{B_1 + B_2} \sinh \left(\frac{H(B_1 + B_2)}{\Theta} \right) \right\} - (\zeta_{11B}^2 B_1 + \zeta_{12B}^2 B_2) \times \left\{ c_- \left[\cosh \left(\frac{H(B_1 - B_2)}{\Theta} \right) - 1 \right] - \frac{s_-}{B_1 - B_2} \sinh \left(\frac{H(B_1 - B_2)}{\Theta} \right) \right\}, \quad (41)$$

where

$$c_{\pm} = (\eta_A \kappa^2 - A_1 A_2) \frac{\zeta_{11B} B_1 \mp \zeta_{12B} B_2}{B_1 B_2},$$

$$s_{\pm} = \pm \frac{1}{2} (B_2^2 - B_1^2) (A_1 + A_2) (B_1 \pm B_2) \left(1 \pm \frac{A_1 A_2}{B_1 B_2} \right).$$

258 Rewriting Eq.(41) as in Appendix Appendix A.1, it is seen that dependence on
 259 $B_{1,2}$ occurs only through even powers, whence only cuts associated with $A_{1,2}$
 260 remain.

When $A = B$, it is

$$(\Gamma, \beta, v, \psi, \eta_B) = (1, 1, 1, \delta, \eta)$$

261 and we retrieve the well expected result

$$D_0^{A=B}(\kappa) = (\zeta_{11A} - \zeta_{12A})^2 (A_1 - A_2) R_A(\kappa),$$

whereby only Rayleigh waves propagate. Similarly, for an exceedingly weak layer, that is for $\Gamma \rightarrow 0$, we find either Rayleigh waves confined to the half-space or RL waves trapped in the free/clamped layer, which bounce off the impenetrable rigid barrier posed by the half-space. In the special case of a vanishing layer, $H = 0$, one gets, to leading order,

$$D_0^{H=0}(\kappa) = (\zeta_{11B} - \zeta_{12B})^2 (A_1 - A_2) R_A(\kappa),$$

262 that gives Rayleigh waves again. Its classical limit (21) gives

$$D_0^{H=0}(\kappa) \rightarrow -\frac{2\delta^2}{\Omega^2} \left(\frac{c_{sB}}{c_{sA}} \right)^4 B_1,$$

263 whence Rayleigh waves collapse onto travelling bulk SH waves. On the opposite
 264 side of the spectrum, for an exceedingly strong layer, that is for $\Gamma \rightarrow +\infty$, we
 265 obtain, as expected, RL modes.

266 4. Wave pattern and microstructural features

267 We now consider the root landscape of $D_0(s)$ considered as a complex-valued
 268 function of the argument $s = \Re(s) + \imath\Im(s)$. Eq.(40) is noteworthy for it shows
 269 that the only branch cuts appearing in $D_0(s)$ are those brought by the Rayleigh
 270 function for the half-space A. Accordingly, in this system, only three families of
 271 waves may exist, namely:

- 272 1. Lamb waves, which are either travelling, when they correspond to the
 273 real zeros of D_0 , or evanescent (Lamb-like waves), characterised by purely
 274 imaginary zeros of D_0 ;
- 275 2. bulk travelling waves, which move like SH bulk waves for the half-space A,
 276 possibly inhomogeneous: these are related to the branch cuts for $A_1(s)$;
- 277 3. bulk standing modes, related to the branch cuts for $A_2(s)$.

278 No bulk modes are possible that are related to SH bulk waves in B.

279 Existence and uniqueness of Love waves may be establish through the argu-
 280 ment principle, following the procedure adopted in Cagniard (1962) and Nobili
 281 et al. (2021) for Stoneley waves, respectively in CE and CS. This technical and
 282 lengthy proof is sketched in Appendix A.2. One major result of this process is
 283 the necessary condition for the existence of Love waves, namely

$$D_0(\delta) \geq 0, \quad (42)$$

284 equality setting the limits of the passbands, i.e. the cut-on and cut-off frequen-
 285 cies. Physically, the passband ends correspond to the situation when Love waves
 286 move with the same phase speed as bulk waves in medium A. In such states,
 287 energy is no longer trapped in the layer, bouncing back and forth between its
 288 boundaries, but leaks in the half-space in the form of bulk waves.

289 Eq.(42) is the fundamental result which enables to relates the band pattern to
 290 the microstructural features in the material. Also, several qualitative outcomes
 291 are possible in dependence of the ratio between the layer and the substrate
 292 microstructure, as it is presently described.

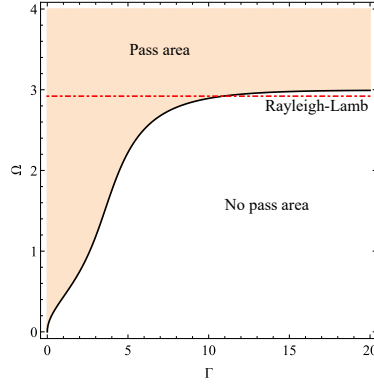


Figure 6: Cut-on frequency vs. shear stiffness ratio Γ for $\ell_A = 0.4 < \ell^B = 0.5$ (solid, black). Propagation occurs above the black curve, which asymptotes to the first symmetric Rayleigh-Lamb mode at the wavenumber $\kappa = \delta$ (red dash-dotted line).

293 4.1. Infinite passbands

294 Fig.6 plots the cut-on frequency as a function of Γ for $\ell_A = 0.4$, which,
 295 for large Γ , asymptotes to the first symmetric RL mode for a free plate at the
 296 wavenumber $\kappa = \delta$. Sweeping larger frequencies reveals a finite passband,
 297 that ranges from cut-on to cut-off, as it is shown in Fig.7. The corresponding
 298 frequency spectrum for Love waves is shown in Fig.8 for $\Gamma = 1$ and $\Gamma = 5$:
 299 the picture confirms that propagation only occurs within a finite frequency
 300 range. It also shows that the dispersive nature of propagation is restricted to
 301 low wavenumbers, a result which was already observed with respect to Rayleigh
 302 waves (Ottosen et al., 2000; Nobili et al., 2019).

303 From the discussion in Sec.3.2, we deduce that an infinite number of pass-
 304 bands is expected: for Γ large, these are framed in between symmetric and
 305 antisymmetric RL modes. Similarly, for $\Gamma = 0$, passbands are constrained by
 306 RL waves propagating in a clamped-free plate at $\kappa = \delta$, that is by the inter-
 307 sections indicated in Fig.5. In fact, the bounding curves for cut-on and cut-off
 308 start at $\Gamma = 0$, which is realized provided that $D_{FC}(\delta) = 0$.

309 4.2. Single passband

310 This propagation landscape, characterized by an infinite succession of pass-
 311 bands, holds only inasmuch as condition (36) stands. Indeed, when micro-inertia

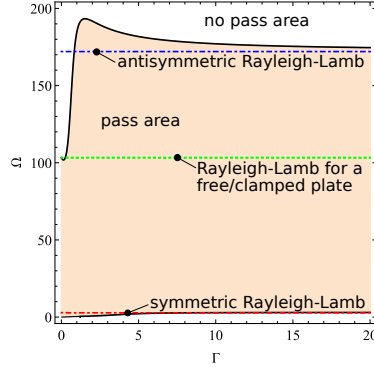


Figure 7: Passband frequency range vs. shear stiffness ratio Γ (solid, black), with $\ell_A = 0.4$. Propagation occurs in the (pink) region in between the black curves; these asymptote to the first symmetric/antisymmetric Rayleigh-Lamb frequencies, respectively for cut-on (red) and cut-off (blue dash-dotted lines). The cut-off curve sets off in correspondence to the occurrence of Rayleigh-Lamb waves in a free/clamped plate (green, dotted)

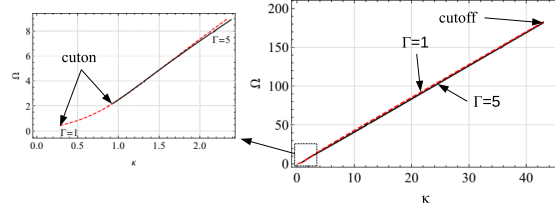


Figure 8: Frequency spectrum for $\Gamma = 1$ (dashed, red) and $\Gamma = 5$ (solid, black) with $\ell_A = 0.4 < \ell^B = 0.5$: Lamb frequency spectra asymptote to Rayleigh waves

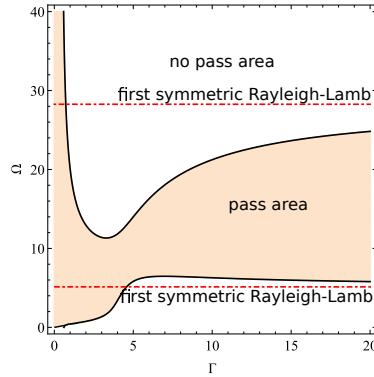


Figure 9: Cut-on frequency vs. shear stiffness ratio Γ for $\ell_A = 0.45$ (solid, black). Propagation occurs between the black curves, which asymptote to two frequencies in the first symmetric Rayleigh-Lamb branch at the wavenumber $\kappa = \delta$ (red dash-dotted lines). Since no intersection with RL waves in a free/clamped plate is possible, cut-off possesses a vertical asymptote

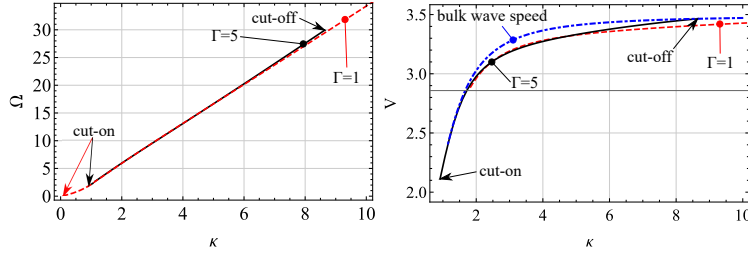


Figure 10: Frequency spectrum (left) for $\Gamma = 1$ (dashed, red) and $\Gamma = 5$ (solid, black), for $\ell_A = 0.45$: only for the latter cut-off is defined. Since spectra almost overlap, dispersion curves are also shown (right) and it is seen that cut-on and cut-off indeed occur at the intersections with the bulk wave speed (dash-dotted, blue)

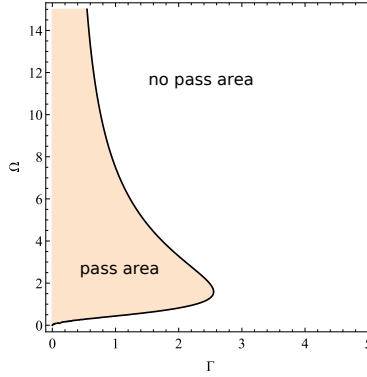


Figure 11: Cut-on frequency vs. shear stiffness ratio Γ for $\ell_A = 0.55 > \ell_B = 0.5$ (solid, black). Propagation occurs up to a limiting threshold for Γ .

312 of medium A is large enough (and therefore bulk waves move slow enough),
 313 propagation occurs through a single passband, which asymptotes to a pair of
 314 frequencies along the first symmetric RL mode, as in Fig.4. This situation is
 315 depicted in Fig.9, that plots cut-on and cut-off frequencies as a function of Γ for
 316 $\ell^A = 0.45$. Since no intersections of bulk waves with RL modes in a clamped/free
 317 plate are possible, cut-off displays a vertical asymptote and, as a consequence,
 318 for Γ small enough, the passband is semi-infinite. The frequency spectrum in
 319 Fig.10 shows that this is indeed the case for $\Gamma = 1$ and yet no longer for $\Gamma = 5$.

320 4.3. Love wave block-band

321 Increasing further micro-inertia in material A, an important change in the
 322 propagation features is encountered: namely the appearance of a bounding curve

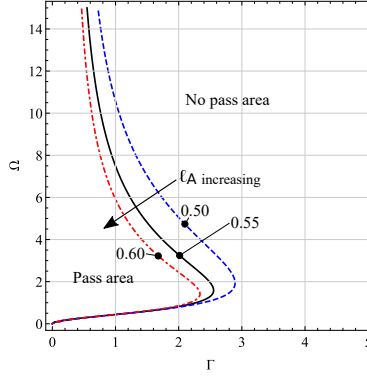


Figure 12: Cut-on frequency vs. shear stiffness ratio Γ for $\ell_A = 0.50$ (dashed, blue), 0.55 (solid, black) and 0.6 (dot-dashed, red): the pass region shrinks as rotational inertia increases in medium A

for Γ . Indeed, since no RL modes in the layer are possible which equally support bulk waves in the half-space, the passband region becomes bounded by $\Gamma < \Gamma_M(\Omega)$, as in Fig.11. This passband region shrinks for larger values of rotational inertia, as illustrated in Fig.12.

5. The classical limits

We now show that neglecting microstructure in only one of either the layer or the half-space generally leads to inconsistencies. Occasionally, however, a special set of boundary conditions is available which lends a well-posed problem.

5.1. Classical layer perfectly bonded to a couple stress half-space

We first consider the case when the layer B is classical elastic and the half-space A is made of couple stress material. This condition is obtained by taking the limit (21) of the general case. We note that, as $\beta \rightarrow 0$,

$$B_1 = \sqrt{\kappa^2 - \frac{\tilde{c}_{sA}}{\tilde{c}_{sB}} \Omega^2 \Theta^2}, \quad B_2 = \frac{\sqrt{2}\Theta}{\beta} + O(1).$$

Then, we can solve Eq.(39b) for o_2 to obtain

$$o_2 = \left[-\frac{\sqrt{2}\Theta}{\beta} \coth \frac{\sqrt{2}H}{\beta} + O(\beta) \right] e_2 + O\left(\frac{\beta}{\sinh(\sqrt{2}H/\beta)} \right), \quad (43)$$

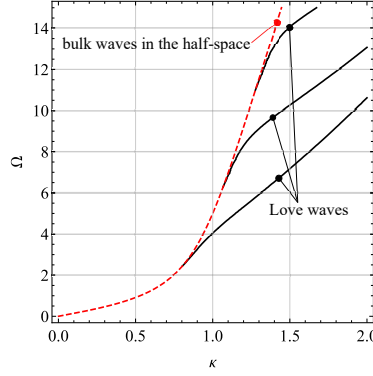


Figure 13: Love waves for a couple stress half-space in perfect contact with a classical layer (solid, black) for $H = 1, \eta_A = 0.5, \ell_A = 0.2, \beta v = 1.5$ and $\Gamma = 3$. For each branch, cut-on is located in correspondence of bulk waves in the half-space (dashed, red).

where the last term is exponentially small. Consequently, rotation continuity (38b) reads

$$o_1 + o_2 - A_1 s_1 - A_2 s_2 = 0,$$

which, assuming all quantities to be $O(1)$, demands $e_2 = O(\beta)$ to eliminate the $O(\beta^{-1})$ term given by o_2 . Solving the remaining equations in the system (38,39) with the assumption $e_2 = 0$, gives the frequency equation

$$-R_A(\kappa) \cosh\left(\frac{B_1 H}{\Theta}\right) + \Gamma \sqrt{2} \Omega^{-1} \delta(A_1 + A_2) B_1 \sinh\left(\frac{B_1 H}{\Theta}\right) = 0, \quad (44)$$

which clearly possesses the structure (40). As Fig.13 shows, this equation is remarkable in that it exhibits an infinite number of branches, which is unexpected for Love waves. Looking at the eigenforms, we find $o_2 = O(1)$, whence the corresponding displacement (30) blows to infinity as $\beta \rightarrow 0$. Also, although e_2 tends to zero, it combines with the exponentially large factor $B_2^{-1} \sinh(B_2 \xi_2) = \frac{\beta}{\sqrt{2}\Theta} \sinh(\sqrt{2}\Theta\beta^{-1}\xi_2)$ to produce an exponentially exploding contribution. As a consequence of these observations, the dispersion relation (44) cannot be directly obtained assuming a classical solution for B and it is thereby defined as non-classical. We also observe that, to leading order, $q_{1A}(0) = 0$, which indeed corresponds to one of the boundary conditions used in Sharma and Kumar (2019); Sharma et al. (2020). However, rotation at the

352 interface is finite and continuous across

$$w'_A(0) = w'_B(0) = \left(A_1 - \frac{\zeta_{12A}}{\zeta_{11A}} A_2 \right) s_1,$$

353 and this condition is neglected.

354 5.2. Couple stress layer perfectly bonded to a classical half-space

Let's now consider the case when A is classical elastic and B is a couple stress layer. Then, $\kappa = O(\beta^{-1})$ and $\Omega = O(v)$, as $\ell_A \rightarrow 0$ and $\beta \rightarrow \infty$, while $v \rightarrow 0$ such that $\beta v < \infty$. Thus,

$$A_1 = \beta^{-1} \sqrt{\kappa_B^2 - \frac{1}{2} \beta^2 v^2 \Omega_B^2} + O(\beta^{-3}), \quad (45a)$$

$$A_2 = 1 + \frac{\kappa_B^2}{2\beta^2} + O(\beta^{-4}), \quad (45b)$$

$$B_1 = \beta^{-1} \sqrt{\kappa_B^2 - \frac{1}{2} \left(\sqrt{(1 - \ell_B^2 \Omega_B^2)^2 + 2\Omega_B^2} - (1 - \ell_B^2 \Omega_B^2) \right)} + O(\beta^{-3}), \quad (45c)$$

$$B_2 = \beta^{-1} \sqrt{\kappa_B^2 + \frac{\Omega_B^2}{\sqrt{(1 - \ell_B^2 \Omega_B^2)^2 + 2\Omega_B^2} - (1 - \ell_B^2 \Omega_B^2)}} + O(\beta^{-3}). \quad (45d)$$

Solving (38d) lends

$$s_2 = \Gamma \left\{ e_1 \left[(\eta_B + 1) \kappa_B^2 + \frac{1}{2} \left(1 - \Omega_B^2 \ell_B^2 - \sqrt{2\Omega_B^2 + (1 - \Omega_B^2 \ell_B^2)^2} \right) \right] \right. \\ \left. + e_2 \left[(\eta_B + 1) \kappa_B^2 + \frac{\Omega_B^2}{\Omega_B^2 \ell_B^2 - 1 + \sqrt{2\Omega_B^2 + (\Omega_B^2 \ell_B^2 - 1)^2}} \right] \right\} + O(\beta^{-2}), \quad (46)$$

355 which, substituted into the remaining set of boundary conditions, yields a system

356 which is singular to leading order, owing to Eq.(39b) disappearing at leading

357 order. Solving any regular subsystem gives

$$o_1 = o_2 = O(\beta^{-1}), \quad \text{and} \quad s_2 = O(\beta^{-2}), \quad (47)$$

358 whereupon, in the limit as $\beta \rightarrow \infty$, the half-space A becomes classical and the

359 layer B admits the even solution only, i.e. $e_1 = e_2 = O(1)$. Consequently,

360 we expect neither rotation nor couple stress in the layer B *to leading order* at

361 the bonding interface $\xi_2 = 0$, for they arise from the odd part of the solution.

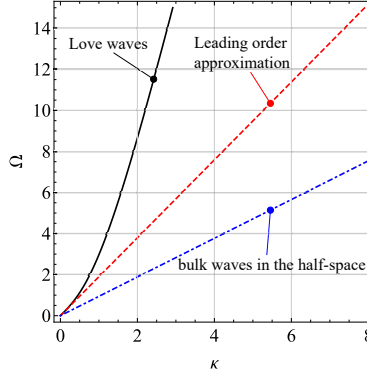


Figure 14: Love wave spectrum when A is classical elastic (solid, black), superposed onto the leading order approximation (49) (dashed, red) for $H_B = 10, \eta_B = 0.8$ and $\ell_B = 0.2$. Bulk waves in the classical half-space $\Omega_B - \sqrt{2}(\beta v)^{-1}\kappa_B = 0$ are also shown (blue, dot-dashed), with $\beta v = 1.5$

Equally, no rotation arises from the half-space A either, because, at $\xi_2 = 0$, it is simply given by

$$A_1 s_1 + A_2 s_2 = O(\beta^{-1}).$$

Thus, rotation continuity is trivially satisfied at leading order. Looking back at couple stress continuity (46), this appears compatible with the last of Eqs.(47) inasmuch as the leading term drops out. Since this is indeed the case, couple stress continuity is also trivially satisfied. Therefore, we are left with the classical system A in perfect contact with the even solution of the couple stress layer B subject to the conditions (38a,38c,39a). Letting $H_B = \beta^{-1}H$, we get the novel frequency equation

$$\zeta_{11B} B_1 \sinh(\sqrt{2}H_B \beta B_1) - \zeta_{12B} B_2 \sinh(\sqrt{2}H_B \beta B_2) = 0, \quad (48)$$

with the understanding that Eqs.(45c,45d) are used to eliminate β . It is observed that terms coming from the half-space A are not present in (48) because they factor out and never contribute a real wavenumber. In this condition, Love waves are always supported as in Fig.14, which also illustrates the leading order approximation

$$\Omega_B^2 = \sqrt{\alpha_1} \kappa_B^2, \quad \alpha_1 = \sqrt{2} \frac{1 - (\eta_B + 1) \frac{\sinh(\sqrt{2}H_B)}{\sqrt{2}H_B}}{1 - \frac{\sinh(\sqrt{2}H_B)}{\sqrt{2}H_B}}. \quad (49)$$

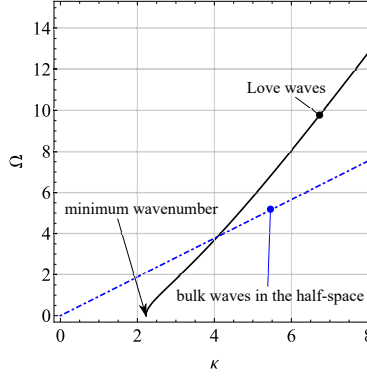


Figure 15: Love wave spectrum when A is classical elastic (solid, black), for $H_B = 2$, $\eta_B = -0.8$ and $\ell_B = 0.2$. Bulk waves in the classical half-space $\Omega_B - \sqrt{2}(\beta v)^{-1}\kappa_B = 0$ are also shown (blue, dot-dashed), with $\beta v = 1.5$

376 With the help of this approximation, it may be shown that, if we can find real
377 solutions of

$$\frac{\sinh(\sqrt{2}H_B)}{\sqrt{2}H_B} = \frac{1}{1 + \eta_B},$$

378 then we get a minimum wavenumber for Love wave propagation, as in Fig.15.

379 It is worth pointing out that various subsets of boundary conditions have
380 been adopted in the literature. As an example, in Fan and Xu (2018), a couple stress layer is perfectly bonded to a classical half-space and the conditions
381 (38a,38c,39) alongside $q_{1A} = 0$ are used instead. Since rotation continuity is
382 missing, the resulting frequency equation does not match (48).
383

384 6. Conclusions

385 We show that incorporating microstructure into the material description
386 leads to a nonclassical band structure for Love wave propagation, which may
387 be conveniently back-processed for non destructive testing (NDT) evaluation of
388 the material microstructure. In particular, an explicit expression is given for
389 the propagation band limits, namely the cut-on and cut-off points. These are
390 shown to correspond to the condition when the localized wave moves with the
391 same speed as the SH bulk wave in the substrate. As a consequence, energy
392 leaks to infinity and it is no longer confined (internal resonance). Precisely

393 this condition may be taken advantage of to assess the mechanical properties
 394 of the two materials by non destructive testing. Indeed, it is simple matter
 395 to experimentally locate cut-on/cut-off frequencies and therefrom compute the
 396 relevant microstructural parameters. In general, the qualitative features of the
 397 band pattern are related to the degree of similarity between the mechanical
 398 properties of the layer and of the substrate.

399 Furthermore, to warrant uniqueness of the inverse problem, multiple ob-
 400 servables needs to be collected, the easiest being the Rayleigh spectrum. In
 401 this context, we show that the frequency equation for Love waves possesses an
 402 elegant three term structure, where Rayleigh and Rayleigh-Lamb modes for a
 403 free and free/clamped layer play an important role. Therefore, consideration
 404 of Rayleigh waves besides Love waves is able to minimize the non-uniqueness
 405 connected to signal back-processing on the surface.

406 Finally, we consider the special situation, well represented in the literature,
 407 as either the substrate or the layer turns classical and therefore has no mi-
 408 crostructure. We show that such glueing of dissimilar material models generally
 409 leads to inconsistencies. Indeed, when the layer microstructure vanishes, the
 410 resulting displacement field grows unbounded. In contrast, the case when the
 411 substrate microstructure becomes exceedingly small still leads to a meaning-
 412 ful solution, which may be obtained directly proceeding from the right set of
 413 boundary conditions. A novel dispersion relation is obtained which lends a
 414 single continuous branch with neither cut-on nor cut-off, as for classical Love
 415 waves.

416 **7. Acknowledgements**

417 The authors acknowledge financial support from POR FESR 2014-2020 ASSE
 418 1 AZIONE 1.2.2, Project IMPReSA, CUP E81F18000310009.

419 **Appendix A. Appendix**

420 *Appendix A.1. Coupling coefficient*

The coupling term in the dispersion relation (40) may be rewritten as

$$D_1(\kappa) = c_c \left[\cosh\left(\frac{HB_1}{\Theta}\right) \cosh\left(\frac{HB_2}{\Theta}\right) - 1 \right] \\ + s_s B_1^{-1} B_2^{-1} \sinh\left(\frac{HB_1}{\Theta}\right) \sinh\left(\frac{HB_2}{\Theta}\right) + (A_1 + A_2) (\zeta_{11B} - \zeta_{12B}) \times \\ \left[s_c B_1^{-1} \sinh\left(\frac{HB_1}{\Theta}\right) \cosh\left(\frac{HB_2}{\Theta}\right) - c_s B_2^{-1} \cosh\left(\frac{HB_1}{\Theta}\right) \sinh\left(\frac{HB_2}{\Theta}\right) \right],$$

with the coefficients

$$c_c = 2\zeta_{11B}\zeta_{12B} (\zeta_{11B} + \zeta_{12B}) (A_1 A_2 - \kappa^2 \eta_A), \\ s_s = -2 (\zeta_{11B}^3 B_1^2 + \zeta_{12B}^3 B_2^2) (A_1 A_2 - \kappa^2 \eta_A), \\ s_c = A_1 A_2 \zeta_{12B}^2 - \zeta_{11B}^2 B_1^2, \\ c_s = A_1 A_2 \zeta_{11B}^2 - \zeta_{12B}^2 B_2^2.$$

421 *Appendix A.2. Existence and uniqueness*

We consider the complex-valued function

$$D(s) = D_0(s) \exp\left(-\frac{2H}{\Theta}|s|\right),$$

422 where the exponential factor is added to obtain algebraic growth as $|s| \rightarrow +\infty$.

423 Indeed, we find that $D(s) \sim |s|^4$ as $|s| \rightarrow \infty$. We recall that $D(s) = D(-s)$ is

424 central-symmetric. The path in the complex plane which is adopted to imple-

425 ment the argument principle is a very large circle of radius $R \rightarrow \infty$ with two

426 pairs of loops: one circles around the branch cuts at $\pm\delta$ and the other around

427 the branch cuts at $\pm i$, both being parallel to the imaginary axis, see Fig.A.16.

428 We thus see that the image of the path γ through the function $D(s)$ circles the

429 origin four times counter-clockwise and, possibly, two time clockwise if condi-

430 tion (42) is violated. In fact, this condition merely states that the image $D(\gamma_\delta)$

431 intersects the real axis to the right of the origin and contributes nothing. In this

432 case we have four roots, a real pair and a complex pair. In contrast, if condition

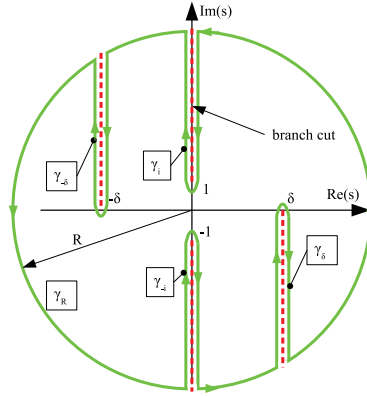


Figure A.16: Path $\gamma = \gamma_R \cup \gamma_{\pm\delta} \cup \gamma_{\pm i}$ for implementing the argument principle: the number of zeros of $D(s)$ equals the number of times the image $D(\gamma)$ winds around the origin

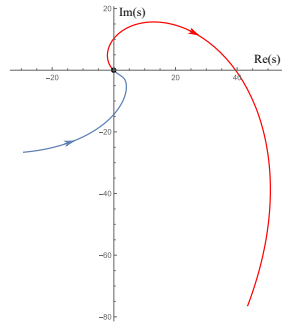


Figure A.17: The image $D(\gamma_\delta)$ winds around the origin in clockwise manner, because $D(\delta) < 0$. Hence, the number of zeros of $D(s)$ is diminished by two

(42) is violated, then the origin sits to the right of path, as in Fig.A.17, and subtracts a pair of roots. Then, only the complex pair remains. It is finally observed that the image $D(\gamma_i)$ never circles the origin.

References

- Achenbach, J., 1984. Wave propagation in elastic solids. volume 16 of *Applied Mathematics and Mechanics*. North-Holland, Elsevier.
- Cagniard, L., 1962. Reflection and refraction of progressive seismic waves. McGraw-Hill.
- Dal Moro, G., 2020. The magnifying effect of a thin shallow stiff layer on Love waves as revealed by multi-component analysis of surface waves. Scientific Reports 10, 1–13.
- Destuynder, P., Fabre, C., 2016. Few remarks on the use of Love waves in non destructive testing. Discrete & Continuous Dynamical Systems - S 9, 427–444.
- Fan, H., Xu, L., 2018. Love wave in a classical linear elastic half-space covered by a surface layer described by the couple stress theory. Acta Mechanica 229, 5121–5132.
- Georgiadis, H., Velgaki, E., 2003. High-frequency Rayleigh waves in materials with micro-structure and couple-stress effects. International Journal of Solids and Structures 40, 2501–2520.
- Gourgiotis, P., Georgiadis, H., 2015. Torsional and SH surface waves in an isotropic and homogenous elastic half-space characterized by the Toupin–Mindlin gradient theory. International Journal of Solids and Structures 62, 217–228.
- Gourgiotis, P., Georgiadis, H., Neocleous, I., 2013. On the reflection of waves in half-spaces of microstructured materials governed by dipolar gradient elasticity. Wave Motion 50, 437–455.

459 Graff, K.F., 1991. Wave motion in elastic solids. Dover Publications Inc., New
460 York.

461 Graff, K.F., Pao, Y.H., 1967. The effects of couple-stresses on the propagation
462 and reflection of plane waves in an elastic half-space. *Journal of Sound and*
463 *Vibration* 6, 217–229.

464 Jin, F., Kishimoto, K., Inoue, H., Tateno, T., 2005. Experimental investigation
465 on the interface properties evaluation in piezoelectric layered structures by
466 Love waves propagation, in: *Key Engineering Materials*, Trans Tech Publ.
467 pp. 807–812.

468 Koiter, W., 1964. Couple-stress in the theory of elasticity, in: *Proc. K. Ned.*
469 *Akad. Wet, North Holland Pub.* pp. 17–44.

470 Lakes, R., 1986. Experimental microelasticity of two porous solids. *International*
471 *Journal of Solids and Structures* 22, 55–63.

472 Li, Y., Wang, W., Wei, P., Wang, C., 2018. Reflection and transmission of
473 elastic waves at an interface with consideration of couple stress and thermal
474 wave effects. *Meccanica* 53, 2921–2938.

475 Love, A., 1911. *Some problems of geodynamics*. Cambridge University Press.

476 Maugin, G., 1988. Shear horizontal surface acoustic waves on solids, in: *Recent*
477 *developments in surface acoustic waves*. Springer, pp. 158–172.

478 Mindlin, R.D., 1964. Micro-structure in linear elasticity. *Archive for Rational*
479 *Mechanics and Analysis* 16, 51–78.

480 Mishuris, G., Piccolroaz, A., Radi, E., 2012. Steady-state propagation of a
481 mode III crack in couple stress elastic materials. *International Journal of*
482 *Engineering Science* 61, 112–128.

483 Nobili, A., Radi, E., Signorini, C., 2020. A new rayleigh-like wave in guided
484 propagation of antiplane waves in couple stress materials. *Proceedings of the*
485 *Royal Society A* 476, 20190822.

486 Nobili, A., Radi, E., Vellender, A., 2019. Diffraction of antiplane shear waves
487 and stress concentration in a cracked couple stress elastic material with micro
488 inertia. *Journal of the Mechanics and Physics of Solids* 124, 663–680.

489 Nobili, A., Volpini, V., Signorini, C., 2021. Antiplane stoneley waves prop-
490 agating at the interface between two couple stress elastic materials. *Acta*
491 *Mechanica* , 1–19.

492 Noble, B., 1958. Methods based on the Wiener-Hopf technique for the solution
493 of partial differential equations, *International Series of Monographs on Pure*
494 *and Applied Mathematics*. Vol. 7. Pergamon Press, New York.

495 Ottosen, N.S., Ristinmaa, M., Ljung, C., 2000. Rayleigh waves obtained by the
496 indeterminate couple-stress theory. *European Journal of Mechanics-A/Solids*
497 19, 929–947.

498 Ray, A., Singh, A., 2020. Love-type waves in couple-stress stratum imperfectly
499 bonded to an irregular viscous substrate. *Acta Mechanica* 231, 101–123.

500 Sengupta, P., Ghosh, B., 1974. Effect of couple-stresses on the propagation of
501 waves in an elastic layer. *pure and applied geophysics* 112, 331–338.

502 Sharma, V., Goyal, R., Kumar, S., 2020. Love waves in a layer with void pores
503 over a microstructural couple stress substrate with corrugated boundary sur-
504 faces. *Journal of the Brazilian Society of Mechanical Sciences and Engineering*
505 42, 1–16.

506 Sharma, V., Kumar, S., 2019. Modelling of love-type waves in an elastic layer
507 sandwiched between viscous liquid half space and size dependent couple stress
508 substrate. *Journal of Theoretical and Applied Mechanics* 57.

509 Shodja, H., Goodarzi, A., Delfani, M., Haftbaradaran, H., 2015. Scattering of an
510 anti-plane shear wave by an embedded cylindrical micro-/nano-fiber within
511 couple stress theory with micro inertia. *International Journal of Solids and*
512 *Structures* 58, 73–90.

- 513 Vardoulakis, I., Georgiadis, H., 1997. Sh surface waves in a homogeneous
514 gradient-elastic half-space with surface energy. *Journal of Elasticity* 47, 147–
515 165.
- 516 Wang, C., Chen, X., Wei, P., Li, Y., 2017. Reflection and transmission of elastic
517 waves through a couple-stress elastic slab sandwiched between two half-spaces.
518 *Acta Mechanica Sinica* 33, 1022–1039.
- 519 Yang, F., Chong, A., Lam, D., Tong, P., 2002. Couple stress based strain
520 gradient theory for elasticity. *International Journal of Solids and Structures*
521 39, 2731–2743.
- 522 Zhang, L., Huang, Y., Chen, J., Hwang, K., 1998. The mode III full-field
523 solution in elastic materials with strain gradient effects. *International Journal*
524 *of Fracture* 92, 325–348.